Du *et al. Biochar* (2026) 8:76
https://doi.org/10.1007/s42773-026-00585-0

Biochar

ORIGINAL RESEARCH Open Access

In-situ and long-enduring oxidation of SMX by Fe-modified biochar activated O_2 in soil: bridging Fe-redox cycling and electron transfer modulation

Hongying Du[1], Lei Zhang[1*], Wenbo Liu[1], Yuyang Xie[1], Xueyan Hou[1], Junkang Guo[1] and Qixing Zhou[2]

Abstract

Hydroxyl radicals (·OH) generated from endogenous Fe(II)/O_2 catalytic system hold substantial potential for the in situ remediation of contaminated farmland, but are substantially constrained by the insufficient Fe-redox cycling. In this study, we designed a Fe-loaded biochar (BC-Fe) that acts as an "electron highway" and a "Fe-redox modulator," enabling the in situ oxidative degradation of sulfamethoxazole (SMX) through the synergistic enhancement of Fe(II)/·OH activation achieved by regulating Fe speciation and electron exchange capacity. Mechanistically, the coexistence of highly reactive surface Fe(II) and optimized electron storage and conductivity establishes a sustainable redox system. This system enables spatiotemporally coupled "charging" (0.5 and 5 M HCl Fe(II) formation and microbial Fe(III)-reduction) and "discharging" (O_2 activation) processes, which collectively promote soil Fe(II) production and Fe phase transformation to drive sustained ·OH production efficiently. Notably, HBC-Fe400 with optimized Fe loading not only minimized the depletion of crystalline Fe(II) in soil and markedly enriched functional genes associated with Fe-redox, but also enabled the synchronized activation of both the direct (BC-Fe-catalyzed) and indirect (soil Fe-redox cycling-amplified) Fenton-like pathways. This dual coordination led to a dramatic 4.2-fold enhancement in ·OH production (881.6 μM), and maintained a 3.58-fold increase under field conditions. Finally, SMX was degraded through three degradation pathways, namely the ring-opening reaction of the isoxazole ring, hydroxylation, and S–N bond cleavage, generating intermediates that contributed to toxicity attenuation. This study provides a sustainable pathway for pollutant degradation by achieving O_2 activation and offers valuable insights for designing advanced Fe-based biochar catalysts in green oxidation processes and environmental remediation.

Highlights

- Fe-based biochar established a sustainable Fe(III)/Fe(II) cycling via a coupled "charging-discharging" mechanism.
- ·OH production surged to 881.6 μM via coupled direct and Fe-cycle amplified Fenton-like pathways.
- SMX degradation reached 81.2% via hydroxylation, isoxazole ring open and S–N bond cleavage.

Keywords Fe-based biochar, Hydroxyl radicals, Fenton-like reaction, Electron transfer, Soil remediation

*Correspondence:
Lei Zhang
zhanglei0954@126.com
Full list of author information is available at the end of the article

Springer

Graphical Abstract

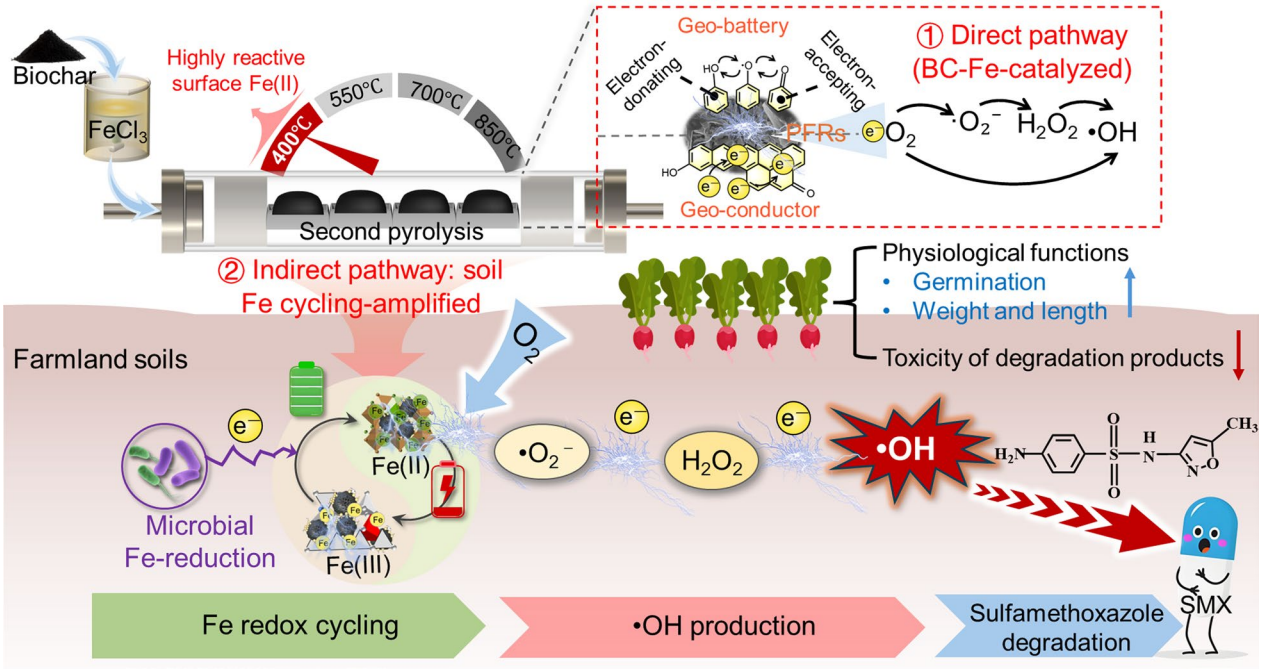

1 Introduction

With the growing demand for remediation of accumulated and emerging organic contaminants, advanced oxidation processes (AOPs) such as ozonation, the Fenton process (Wei et al. 2025), and persulfate-based oxidation have attracted considerable attention and found widespread application. However, these oxidative treatments primarily target high-concentration organic contaminants in wastewater, sludge, and contaminated site soils. The exogenous introduction of strong oxidants may significantly disrupt the intrinsic properties and ecological functions of native soil systems, making them unsuitable for degrading trace or micro-organic pollutants in agricultural soils. In contrast, naturally abundant molecular oxygen (O_2) presents a more environmentally friendly and cost-effective alternative to conventional oxidants. Recent studies have demonstrated that Fe(II)-bearing minerals can activate O_2 to generate reactive oxygen species (ROS), particularly ·OH ($E^0 = 2.8$ V), which play crucial roles in regulating element cycles (Yang et al. 2025), microbial activity (Liu et al. 2024d), and pollutants dynamics. Given the ubiquitous distribution of Fe-containing minerals in natural soils, the endogenous Fe(II)/O_2 system represents a promising and sustainable strategy for the in situ remediation of contaminated farmland, minimizing reliance on external chemicals while helping to preserve soil ecological integrity.

Fundamentally, the efficacy of this endogenous system hinges on a fundamental process: the transfer of electrons from reduced substances to O_2, which represents a pivotal pathway for ROS production in soil (Liu et al. 2024c), especially in environments with frequent redox fluctuations (e.g., intertidal wetlands (Liu et al. 2024a), riverbanks (Zhao et al. 2023), and rice paddies (Huang et al. b)) and redox-active microdomains. However, the efficiency of the Fe-containing mineral-based Fenton-like catalytic system is constrained by sluggish Fe(III)/Fe(II) redox cycles (Xiao et al. 2021), resulting in low ·OH yields under natural soil conditions. Mounting studies have demonstrated that the application of soil amendments, particularly pyrolysis-derived biochar (BC), has emerged as a promising solution (Wang et al. 2021; Yang et al. 2023). For instance, Huang et al. (2023a) reported that pyrogenic carbon (PyC) accelerated Fe(II)/Fe(III) cycling and ·OH production during redox fluctuations of paddy soils. Another study also revealed that the addition of BC to a Fenton system increased ·OH yield by 2.08-fold (Wang et al. 2025a).These improvements are attributed to two inherent characteristics of BC: (1) It exhibits high redox activity, enabling the storage of 0.3–2.3 mmol

e^{-} gC^{-1} (Amen et al. 2020; Li et al. 2024c); (2) Its high electrical conductivity of the graphitized structure facilitates rapid electron migration across different energy bands and interfaces, thereby constructing efficient electron transfer networks (Yang et al. 2021). Nevertheless, a critical and persistent challenge remains: most existing biochar materials struggle to simultaneously optimize and synergize high redox activity with high electron conductivity. Enhancing one property often comes at the expense of the other, thus limiting the overall efficiency in promoting the Fe(III)/Fe(II) cycle. Achieving this synergistic enhancement is therefore a pivotal breakthrough needed for developing effective endogenous remediation technologies.

To address this, we developed a novel Fe-based biochar platform that enables tailored, synergistic regulation of Fe(II) speciation and carbon-phase electron conductivity via the interactions between active Fe species and the carbon matrix (Chen et al. 2020), thereby facilitating efficient, sustained ·OH generation to accelerate the in situ degradation of organic pollutants. Specifically, Fe-containing minerals with varying crystallinity exhibit significant differences in their surface active sites and catalytic activity (Yu et al. 2024). Poorly crystalline Fe-containing minerals exhibit a highly active surface Fe(II) that enables rapid participation in redox reactions (Huang et al. 2021). Meanwhile, crystalline minerals like magnetite (Fe_3O_4) contains both structural Fe(II) and Fe(III) (Duan et al. 2025; Meng et al. 2024; Tao et al. 2019), which can serve as a stable electron source for Fe-redox cycling activation, thereby facilitating continuous Fenton-like reactions and ·OH production in soil via self-sustained electron transfer over an extended period (Li et al. 2024b). For instance, Wei et al., (2025) developed Fe-enriched biochar from Fe-rich sludge that effectively removed 4-chlorophenol (4-CP) through a Fenton-like reaction, demonstrating its role as a sustained Fe(II) source with excellent performance over multiple cycles. Therefore, we hypothesize that this tailored design will create a coupled "charging-discharging" system: the carbon phase facilitates efficient electron transfer ("conductivity") and storage ("redox activity"), while the engineered Fe species (e.g., poorly crystalline phases for high reactivity and crystalline magnetite for stable electron supply) ensure a sustained source of reactive Fe(II). This synergy is anticipated to robustly drive the Fe(III)/Fe(II) cycle and enable sustained O_2 activation for efficient ·OH production. Notably, the synergistic effects of Fe speciation and carbon phase on both the priming effect for Fe-redox cycling and ·OH production, as well as on the dynamics and activity of soil microbial communities in amended soils, require further in-depth exploration.

Herein, this study proposes a "waste-to-remediation" strategy by developing a novel Fe-modified biochar (BC-Fe) catalyst via a unique pyrolysis-impregnation-pyrolysis method. This synthesis approach is designed to synergistically enhance both the redox activity and electrical conductivity of BC substrate, thereby improving Fe(II) species regulation and electron transfer for efficient O_2 activation in a Fenton-like system, targeting the removal of Sulfamethoxazole (SMX), a representative antibiotic commonly detected in agricultural soils. The specific objectives of this study are: (i) to elucidate Fe phase transformation and ·OH production associated with the activation effects of catalytic amendments on Fenton-like reaction systems, (ii) to decipher the biotic-abiotic electron transfer mechanisms mediated by BC-Fe in Fenton-like systems via integrated electrochemical analysis, microbial community analysis, and correlation studies, and (iii) to validate SMX degradation dynamics through plant simulation and toxicity prediction experiments. Our results are expected to advance the field of O_2 activation and provide guidance for ·OH production in BC-Fe systems, thereby paving the way for novel *in-situ* remediation technologies that improve the productivity and safety of sustainable agriculture.

2 Materials and methods

2.1 Preparation of Fe-enriched biochar

Comprehensive details about the chemicals used in this study are provided in Supplementary Material Text S1. A blend of locally available waste sawdust, gathered from a wood processing facility, was chosen as the raw biomass material. A series of BC-Fe materials with diverse Fe(II) activities and varying electron transfer capabilities were prepared through a novel pyrolysis-impregnation-pyrolysis method. The initial pyrolysis of Fe-free sawdust primarily regulates the graphitization degree and redox characteristics of the resultant biochar, while the secondary pyrolysis process is mainly responsible for modifying the speciation and activity of Fe (Xu et al. 2022). The specific preparation protocol is shown in Fig. S1. Initially, pristine biochar was prepared by slow pyrolysis of sawdust at 400 °C for 1 h in a nitrogen(N_2) atmosphere, then dried and added to a ferric chloride ($FeCl_3$) solution, with the mass ratios of biochar to Fe set at 10:1, 5:1, and 1:1. Each mixture was stirred using a magnetic stirrer at 300 rpm for 24 h, followed by drying and a second pyrolysis under an N_2 atmosphere for 1 h at 400, 550, 700, and 850 ℃. The resulting Fe-biochar composites are designated BC-Fex, where "x" represents the second pyrolysis temperature (BC-Fe400; BC-Fe550; BC-Fe700; BC-Fe850 and LBC-Fe400, BC:Fe = 10:1; MBC-Fe400, BC:Fe = 5:1;

HBC-Fe400, BC:Fe = 1:1). The characterization methods for the morphological characteristics, structural and physicochemical properties, persistent free radicals (PFRs), and electrochemical properties of BC-Fex are described in Text S2-S3.

2.2 Soil anoxic-aerobic incubation

The physicochemical properties of the soil are provided in Table S1, and the experimental process of soil reduction-reoxidation is illustrated in Fig. 1a. Before oxygenation, the farmland soils were incubated in the dark at room temperature for a week under anoxic conditions to reconstitute their microbial activity (especially Fe-reducing) and establish equilibrium conditions (Chen et al. 2021). Briefly, farmland soils were weighed into 100 mL serum bottles, to achieve a well-mixed system consisting of 47.5 g of soil (dry weight), 15 mL of deoxygenated deionized water, and 2.5 g (5%, w/w) BC-Fex. These bottles were sealed with aluminum caps and rubber stoppers inside an anoxic glovebox (Braun Co., Germany) for anoxic incubation. Parallel control experiments, excluding BC-Fex, were conducted under identical conditions. A week later, the rubber stoppers and aluminum caps of the serum bottles were removed, and the bottles were then placed under natural aerobic conditions to continue the oxygenation experiments. All experiments were carried out under a controlled ambient temperature of 25 ± 0.5 ℃. At predetermined time points, samples were collected for the analysis of a series of physicochemical indicators, ·OH, Fe speciation, and SMX determination. Detailed protocols for preparing SMX-contaminated soil and quantifying SMX concentrations in soil are provided in Text S4-S5.

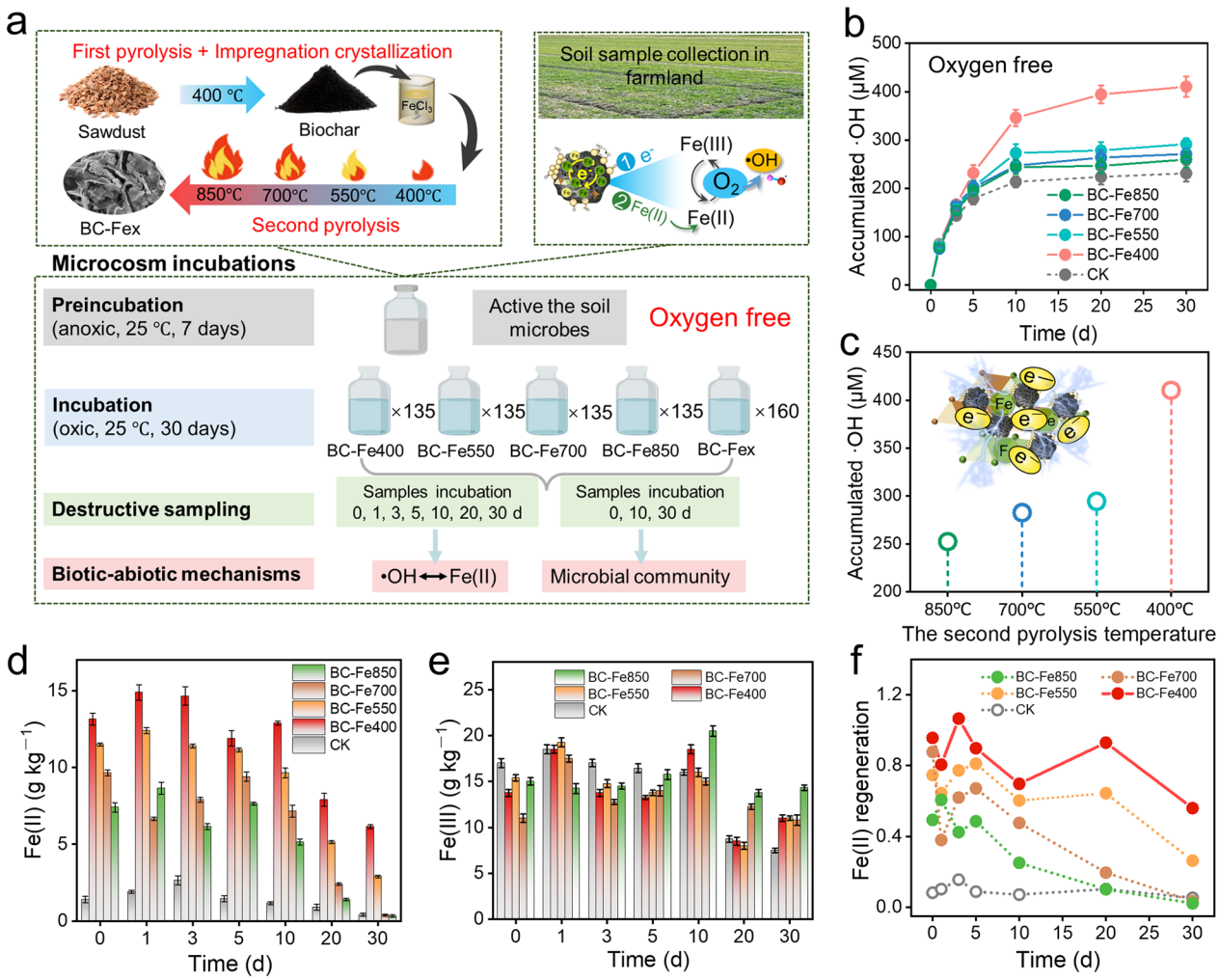

Fig. 1 **a** Experimental schematic. **b**, **c** Secondary pyrolysis temperature-governed ·OH production from BC-Fex in soil. The content of **d** Fe(II) and **e** Fe(III) during oxygenation of soils with/without BC-Fex. **f** Fe(II) regeneration ratio. Error bars indicate the standard error of three replicates.

2.3 ·OH production assessments

To quantify ·OH production under O_2-saturated conditions, 0.1 g soil samples were rapidly mixed with 1.0 mL of 10 mM oxygenated sodium benzoate (BA) (Huang et al. 2023b), resulting in a BA dosage of 10 μmol per sample. At set time points, 0.5 mL aliquots were instantly combined with 0.5 mL of methanol to scavenge ·OH, followed by filtration through a 0.22 μm membrane. The resulting filtrates were analyzed for *p*-hydroxybenzoic acid (*p*-HBA) using high-performance liquid chromatography (HPLC, Agilent, USA) (Text S6). The production of *p*-HBA was used to estimate ·OH production via a conversion factor of 5.87 (Xie et al. 2021).

2.4 Activation of Fe-redox cycling analysis

A sequential extraction approach was used to explore the redox dynamics of Fe(II) species during the incubation of soil oxidation. A certain amount of fresh soil was sequentially extracted using 0.5 M HCl, 5 M HCl, and 1.8 M H_2SO_4 with 1.3 M HF to obtain three types of Fe phases including (i) surface-bound/complexed Fe and Fe in low-crystalline minerals, (ii) high-crystalline Fe-bearing minerals, and (iii) Fe in silicates and clays, respectively, which was measured at 510 nm with a microplate reader (Tecan Infinite 200 Pro, Switzerland) using the 1,10-phenanthroline method (Huang et al. 2023a). Furthermore, ^{57}Fe Mössbauer spectroscopy was employed to analyze freeze-dried samples, aiming to investigate the transformation of Fe species (Text S7).

2.5 Microbial analysis and phytotoxicity test

To access the effects of BC-Fex on soil microbial communities, 1 g of soil was centrifuged at 14,000 × *g* for 1 min at 4 °C. Total microbial DNA was extracted using the Fast DNA™ SPIN Kit for Soil (MP Biomedicals, Irvine, California USA). The quality and concentration of the extracted total DNA were determined via NanoDrop2000 spectrophotometry (Thermo Scientific, USA). The V3-V4 region of 16S rRNA genes was amplified with the universal primer 338F (5' -ACTCCTACG-GGAGGCAGCAG-3') and 806 R (5' -GGACTACHVGGGTWTCTAAT- 3') (He et al. 2024). Purified PCR products were subsequently subjected to high-throughput sequencing on the Illumina MiSeq platform (Illumina Inc., San Diego, USA). Detailed Phytotoxicity test methods are provided in Text S8.

2.6 Statistical analysis

All data were expressed as the mean ± the standard deviation of three replicates. An analysis of variance with Tukey's tests in IBM SPSS Statistics 20 was conducted to detect significant mean differences at $p < 0.05$. A Mantel test analysis was conducted to examine the relationship between physicochemical and electrochemical properties of BC-Fex and ROS production. The relative importance of various factors in ·OH production was quantified via Random Forest (RF) analysis. RF analysis was performed using the R packages "randomForest", "randomForestExplainer", and "rfPermute" in the R Statistical Environment (Version 4.1.1, R Core Team). Structural equation modeling (SEM) was conducted to establish causal pathways among environmental factors and ROS dynamics, which was carried out using Amos 20.0 software (IBM Corporation Software Group, Somers, NY). The modeling process of SEM is provided in Text S9. Other's specific indicators were calculated and graphed by Origin 2022.

3 Results and discussion

3.1 Promoted ·OH production from BC-Fex-mediated oxidation in soil

Given the critical role of ·OH in contaminant degradation, we systematically evaluated ·OH production in soils amended with BC-Fex. The influence of the secondary pyrolysis temperature on ·OH generation was initially assessed (Fig. 1b, c). All amended samples exhibited significantly accelerated ·OH production, with rapid accumulation during the initial 10 days (213.5–345.8 μM) and a slower rate from 10 to 30 days (259.5–416.5 μM). The highest cumulative ·OH yield was achieved in BC-Fe400-amended soil, highlighting the crucial role of the intrinsic redox activity of carbon substrate as a ·OH "priming pump". Furthermore, this temperature-dependent ·OH production corresponds to the variations in oxygen-containing functional groups present in BC-Fe as the second pyrolysis temperature changes.

Notably, as a potential source for supplementing soil Fe nutrition, BC-Fex significantly enhanced the total Fe (TFe) content in soil, with BC-Fe400 demonstrating the most pronounced effect by increasing it by 28.5–45.6% (Fig. S2). Furthermore, although Fe(II) generally exhibited a decreasing trend during the prolonged incubation, the Fe(II) content in BC-Fe400 was much higher than that in CK (1.4–2.2 g kg^{-1}), reaching 17.6–18.9 g kg^{-1} within the first three days of incubation. Even after 30 days, it remained at 6.8 g kg^{-1}, while that in CK, BC-Fe700, and BC-Fe850 had all declined to less than 1 g kg^{-1} (Fig. 1d). Notably, the Fe(III) content in BC-Fe400 was nearly the lowest across all treatments, while it exhibited the highest Fe(II) regeneration

ratio (Fig. 1e, f). These collective findings suggest that BC-Fe400 possessed an outstanding capacity for Fe reduction activation, which was likely to efficiently promote soil Fe redox cycling and provide long-acting sustained-release of active Fe(II), thereby facilitating highly efficient ·OH production(Huang et al. 2023a; Zhang et al. 2022).

3.2 Critical role of BC-Fex physico-electrochemical properties in ·OH production

3.2.1 Fe-phase evolution characteristics

Following the designed fabrication process, Fe species were deeply embedded within the carbon network structure of the biochar, and the total Fe contents in the obtained BC-Fex ranged between 70.8 and 101.4 mg g^{-1} (Fig. 2a and Table S2). Additionally, XRD analysis revealed the presence of diverse Fe species (Fig. 2b). Given that the labile carbon in biochar produced at the initial low pyrolysis temperature (400 °C) promoted the Fe anchoring and production of reductive Fe species, a lower second pyrolysis temperature facilitated the formation of magnetite (Fe_3O_4, PDF#01-1111) (Xu et al. 2020) and hematite (Fe_2O_3, PDF#24-0072). Notably, reduced Fe species (FeO) were only observed in BC-Fe400 and BC-Fe500, while Fe_3O_4, protected by the graphite carbon shell layer, underwent significant

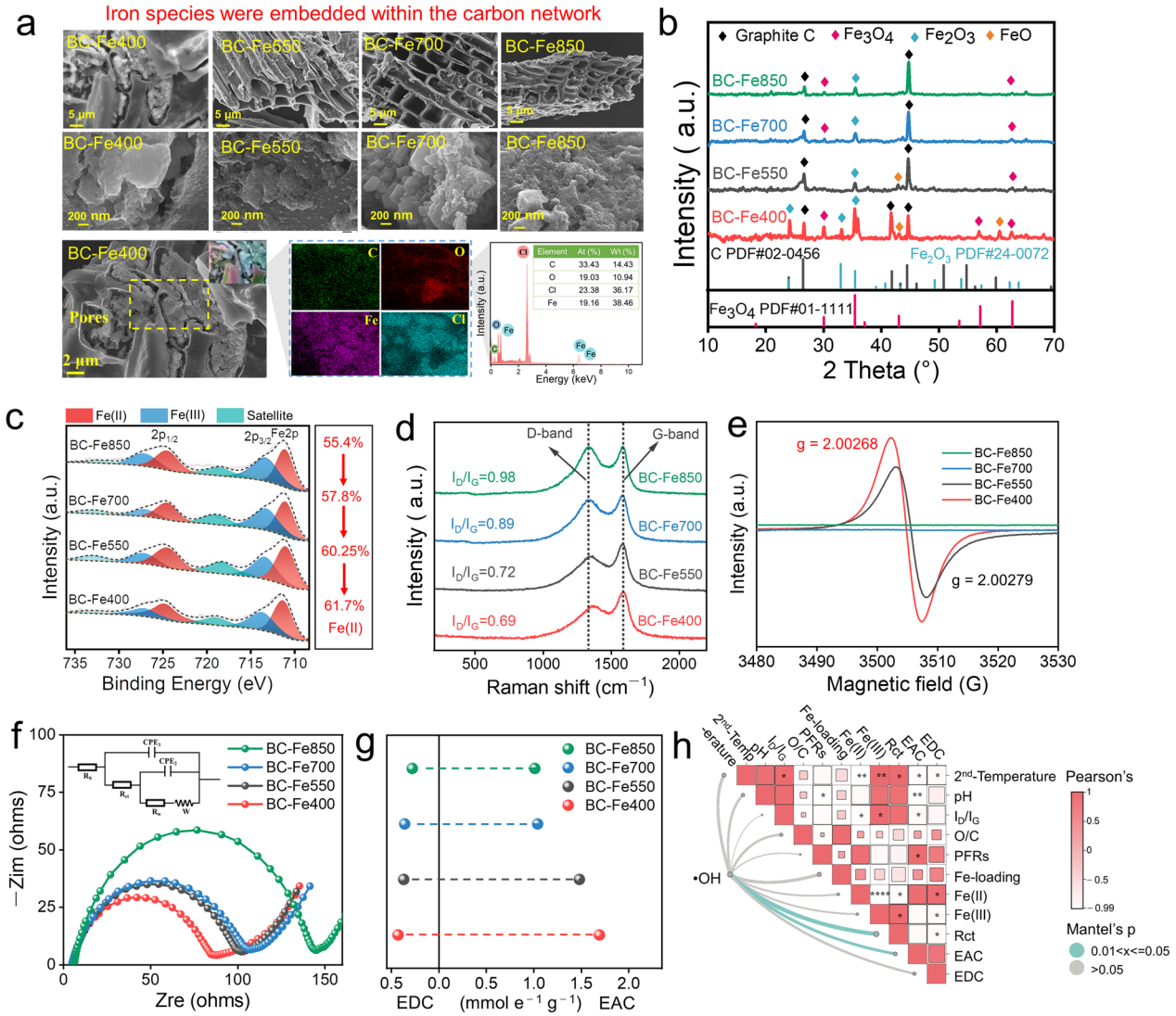

Fig. 2 **a** SEM images and corresponding elemental mapping of BC-Fex. **b** XRD patterns. **c** Fe 2p of XPS spectrum. **d** Raman spectra. **e** EPR signals of PFRs. **f** EIS curves. **g** Electron-donating capacity (EDC) and electron-accepting capacity (EAC). **h** Mantel correlations of the soil ·OH formation with properties of BC-Fex.

chemical reactions accompanied by a decrease in Fe loading at 700 and 850 °C. Correspondingly, the XPS Fe 2p spectra(Fig. 2c) revealed an increase in the Fe(II) proportion from 55.4% to 61.7% in BC-Fe850 and BC-Fe400, further indicating a promoted Fe reduction process. Furthermore, the characterization results suggest that a higher Fe loading is more favorable for the production of Fe_3O_4 and reductive FeO species (Huang et al. 2024; Zhu et al. 2024), as evidenced by the increased Fe(II) content reaching 74.6% in HBC-Fe400 (Figs. S3, S4).

3.2.2 C-based electron transfer capacity

With respect to the carbon structure, joint Raman-FTIR-XPS analyses of BC-Fex revealed that with increasing secondary pyrolysis temperature, the I_D/I_G ratio rose from 0.69 to 0.98, surface functionality diminished, and the O/C atomic ratio decreased from 0.24 to 0.17 (Fig. 2d and S5a), while C-centered PFRs exhibited a g-factor of up to 2.00279 (Fig. 2e). These observations suggest a progressive enhancement in graphitization and structural defects due to the breaking of chemical bonds at higher temperatures, as well as Fe-induced distortion of basal planes during co-pyrolysis (McDonald-Wharry et al. 2013; Xia et al. 2023). Interestingly, according to the CV (Fig. S6) and EIS (Fig. 2f), BC-Fe400 exhibited the highest electrical conductivity, as indicated by its low charge transfer resistance (Rct = 76.8 Ω), whereas BC-Fe850 showed a significant decrease in conductivity, with Rct increasing to 135.8 Ω. This decline is likely attributed to the higher density of insulating sp^3/vacancy defects that surpass the percolation threshold. Furthermore, the redox activity-related electron exchange capacity (EEC, EEC = EAC + EDC) exhibited a pronounced temperature dependence: BC-Fe400 attained the highest EEC value of 2.12 mmol e^{-1} g^{-1}, with corresponding EAC and EDC values of 1.69 and 0.43 mmol e^{-1} g^{-1}, respectively (Fig. 2g). The detailed calculation procedures for EAC and EDC are provided in Text S3 of the Supplementary Information. Predictably, the unique structure-balanced graphitic order and surface functionality of BC-Fe400 achieved an optimized balance between electronic storage capacity and conductivity, which can synergistically enhance electron transfer efficiency during Fenton-like reactions for ·OH production.

Furthermore, Mantel test results revealed a strong correlation ($p < 0.05$) between ·OH production and EAC as well as Rct for BC-Fex-mediated reactions (Fig. 2h). Meanwhile, Fe-loading and Fe(II) content exhibited significant positive/negative correlation with EAC (r = 0.64–0.95) and Rct (r = −0.67 to 0.96), respectively. This demonstrates that pyrolysis-tailored Fe(II) speciation directly regulates redox cycles, while electron transfer capacity underpins the kinetic feasibility of ·OH production. These elements synergistically dictate BC-Fex-mediated ·OH production.

3.3 ·OH production and Fe transformation in soil amended with different Fe-loading capacity on BC-Fe400

3.3.1 ·OH production in soil amended with different Fe-loading capacity on BC-Fe400

The promoting effect of Fe-loading on ·OH production was evident, as demonstrated by BC-Fe400, which exhibited a 1.6-fold increase compared to pristine biochar (BC400, 256.9 μM, Fig. S7a) after a 30-day incubation. Correspondingly, for BC-Fe400 with varying Fe loading, it was evident that an increase in both Fe loading and Fe(II) content resulted in a sharp rise in ·OH production (Fig. 3a, b). Specifically, ·OH production rose from 416.5 μM in LBC-Fe400 (3.1% Fe loading, 61.7% Fe(II)), to 712.9 μM in MBC-Fe400 (7.5% Fe loading, 64.1% Fe(II)), and further reached 881.6 μM in HBC-Fe400 (10.5% Fe loading, 74.6% Fe(II)). This pronounced enhancement was likely attributed to synergistic effect of the "direct" catalysis by BC-Fe and "indirect" oxidation mediated by soil Fe-redox cycling. The production of ·OH radicals was further verified by the characteristic EPR spectrum, featuring four equally spaced lines with a peak intensity ratio of 1:2:2:1 (Liu et al. 2024b). The simultaneous detection of $\cdot O_2^-$ provided evidence for its role as an intermediate precursor in Fe-mediated ·OH production (Han et al. 2022) (Fig. S7b). Moreover, the decrease in ·OH production under water-saturated conditions (43.1%) and in the dark (12.2%) (Fig. 3c), suggested that BC-Fe-mediated ·OH production was primarily driven by sufficient ambient dissolved O_2. Notably, the soil amended with HBC-Fe400 maintained a 3.58-fold increase in ·OH production under field conditions(Fig. S7c).

3.3.2 Oxidation of Fe(II) species in soils incubation

The distributional changes of Fe(II) species in soil amended with BC-Fe400 with varying Fe loadings were further elucidated through stepwise extraction analysis. A progressive decline in TFe(II) extracted with both 0.5M and 5M HCl was observed as the incubation progressed. In contrast, the level of HF-extractable TFe(II) began to increase beyond day 20(Fig. 3d–f). As shown in Fig. 3g, after 30-day incubation, the content of 0.5 M HCl Fe(II) in BC-Fe400 increased with higher Fe loading, reaching 0.33 g kg^{-1} in HBC-Fe400. In contrast, the content of 5 M HCl-extractable Fe(II) in HBC-Fe400 was lower than that in MBC-Fe400 and LBC-Fe400 (Fig. 3h). These results suggested that a higher Fe loading was more conducive

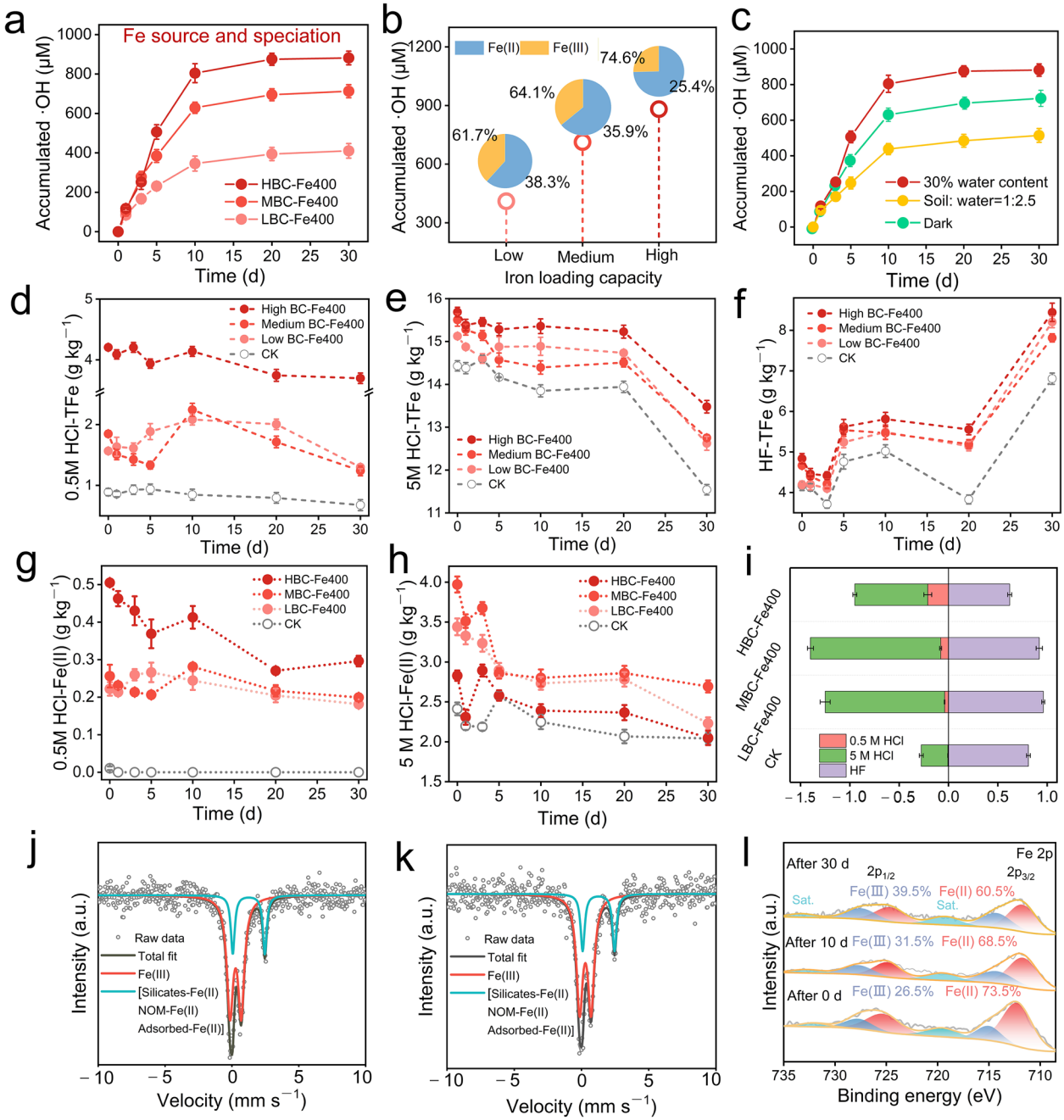

Fig. 3 **a**, **b** ·OH production in soil with BC-Fe400 of different Fe-loading capacity. **c** ·OH production in soil amended with HBC-Fe400 under varied environmental conditions. **d**–**f** Changes in extractable Fe(II) species (0.5M HCl-Fe(II),5M HCl-Fe(II) and HF-Fe(II) in soil with/without HBC-Fe400. **g**, **h** Changes in extractable Fe(II) species (0.5M HCl-Fe(II) and 5M HCl-Fe(II) in soil with/without HBC-Fe400. **i** Changes in oxidated Fe(II) species in soils with/without HBC-Fe400 after 30-d incubation. **j**, **k** Mössbauer spectra of HBC-Fe400 before (0 day) and after oxygenation (30d). **l** Evolution of Fe2p spectra after soil was amended (0–30d) with HBC-Fe400. Error bars indicate the standard error of three replicates

to promoting the formation of active Fe(II) in soil, particularly the 0.5 M HCl Fe(II) (ThomasArrigo et al. 2024).

During oxygenation, complete oxidation of the 0.5M HCl-Fe(II) species was observed within 24 h in the CK, whereas that content decreased from 0.49 to 0.30 g kg^{-1} in HBC-Fe400 after 30 d. A similar tendency was observed for 5M HCl-Fe(II), with oxide-associated Fe(II) ranging from 0.78 to 1.28 g kg^{-1} across all treatments. These results indicated that both 0.5M and 5M HCl-Fe(II) acted as active Fe(II) species during the

oxygenation process in our experiments. However, correlation analyses suggested that the contribution of 0.5M HCl-Fe(II) ($R^2 = 0.81$, Fig. S8) to ·OH accumulation was greater than that of 5M HCl-Fe(II) ($R^2 = 0.55$). Given that the content of 0.5M HCl-Fe(II) in HBC-Fe400 was significantly higher than in other treatments (Fig. 3i), the findings imply that surface-exposed Fe(II) may be regenerated during oxygenation, thereby slowing the oxidation rate of Fe(II). Additionally, the HF-Fe(II) content in all treatments exhibited an overall upward trend after 20 days, with the Fe loading enhancing this increase (Fig. S9). This demonstrates that low-crystalline Fe(II) undergoes transformation and accumulates into secondary high-crystalline minerals (including Fe(III)/Fe(II) mixed minerals and Fe(II) minerals (Si et al. 2024)) after oxidation. This transformation was attributed to the higher EEC of BC-Fe400 for redox cycling and Fe species transformation, thereby resulting in a decrease in both the Fe(II) oxidation rate and ·OH production during 20–30 d.

Furthermore, Mössbauer spectroscopy indicated a slight decrease in the Fe(II) phase from 27.9% to 24.6% in HBC-Fe400 after 30 d incubation, meanwhile XPS revealed a decrease in the surface Fe(II) from 73.5% to 60.5% (Fig. 3j–l and S10). The oxidation losses were significantly lower than the reduction measured by chemical extraction, which confirmed the sustainable regeneration of surface-oxidized Fe(II) species, probably attributed to the electron-transfer capacity of biochar that promoted the release of electrons stored within Fe(II) minerals or structural frameworks. In summary, our integrated analysis reveals a sequential transformation path during the 'charging-discharging' cycle: (i) the rapid 'discharging' of surface 0.5M HCl-Fe(II) for ·OH production; (ii) the concurrent 'charging' of the surface via electron transfer from the 5M HCl-Fe(II) reservoir in the bulk, as evidenced by the disparity between XPS and Mössbauer data; and (iii) the long-term sequestration of Fe into stable HF-extractable phases. Overall, during oxygenation, surface-exposed Fe(II) in BC-Fe400 was primarily oxidized, followed by the transport of interior electrons to the surface-exposed Fe, potentially facilitated through bacterial-biochar-mineral associations via geobattery-like conductive network. The aforementioned results demonstrated that BC-Fe400 can effectively promote the Fe(III)/Fe(II) redox cycling in soil by the sustained supply of reactive Fe(II), thereby overcoming the key limitations of the Fe(II)/O_2 system.

3.4 Response of microbial communities and Fe(III)-reduction activity

Soil bacteria serve as important sources of $\cdot O_2^-$ and H_2O_2 (Han et al. 2022; Wang et al. 2025b). Importantly, these microorganisms can not only directly influence ·OH production by modulating the production of $\cdot O_2^-$ but also indirectly regulate it by facilitating Fe redox cycling (Shen et al. 2025; Wan et al. 2022). During the soil incubation, the cumulative ·OH production was 881.6 μM in the HBC-Fe400 treatment but decreased to 533.0 μM in the sterilized treatment. This indicates that microbially mediated processes account for approximately 39.5% (348.6 μM) of the total ·OH generation, whereas abiotic pathways (primarily the intrinsic Fenton-like activity of HBC-Fe400) contribute about 60.5% (533.0 μM) (Fig. 4a) (Chi et al. 2024). To further elucidate the effects of HBC-Fe400 on microbial functionality and community diversity, high-throughput sequencing was performed after incubation. HBC-Fe400-10d exhibited the highest proportion of unique genera, indicating a potential for transient niche specialization (Fig. 4b). Principal coordinate analysis (PCoA) analysis (Fig. 4c) revealed significant separation among different treatments, indicating that HBC-Fe400 significantly altered the microbial communities. Meanwhile, soils amended with HBC-Fe400 exhibited a significant increased bacterial α-diversity after 30-d incubation (Fig. 4d), with a rapid decline in Eh (Fig. S11), compared to CK, suggesting greater ecosystem stability and stronger resistance capacity within the restoration process.

Specifically, the bacterial community composition was predominantly characterized by the phyla Firmicutes, Proteobacteria, and Actinobacteria (Fig. 4e). Notably, the application of HBC-Fe400 decreased the relative abundance of Firmicutes while promoting the growth of Proteobacteria, and Actinobacteria (copiotroph, *r*-strategists), which accounted for 13.5% and 12.1%, respectively, after 30-d incubation. These phyla thrive better in nutrient-rich habitats and are well recognized for their efficient aerobic degradation of various labile and complex organic compounds, which also exhibited increased abundance in soils amended with HBC-Fe400. Furthermore, soils treated with HBC-Fe400 exhibited a higher relative abundance of Fe-reducing bacteria than those without HBC-Fe400 input. Among the most abundant genera, *Bacillus*, *Geobacter*, *Pelobacter* and *Rhodobacter* have been identified as the primary Fe(III)-reducing bacterial group (Fig. 4f).

Furthermore, to illustrate the symbiotic relationships and niche distribution within soil microbial communities under HBC-Fe400 treatments, the top 20 bacterial genera with the highest abundance were selected to build microbial interaction networks (Fig. 4g, h). Compared with the CK, the HBC-Fe400-amended soil exhibited a greater number of connections and higher edge density, as evidenced by an increase in the average degree from 2.84 (CK) to 4.95, along with a 25% decrease in modularity, suggesting decreased niche partitioning and more

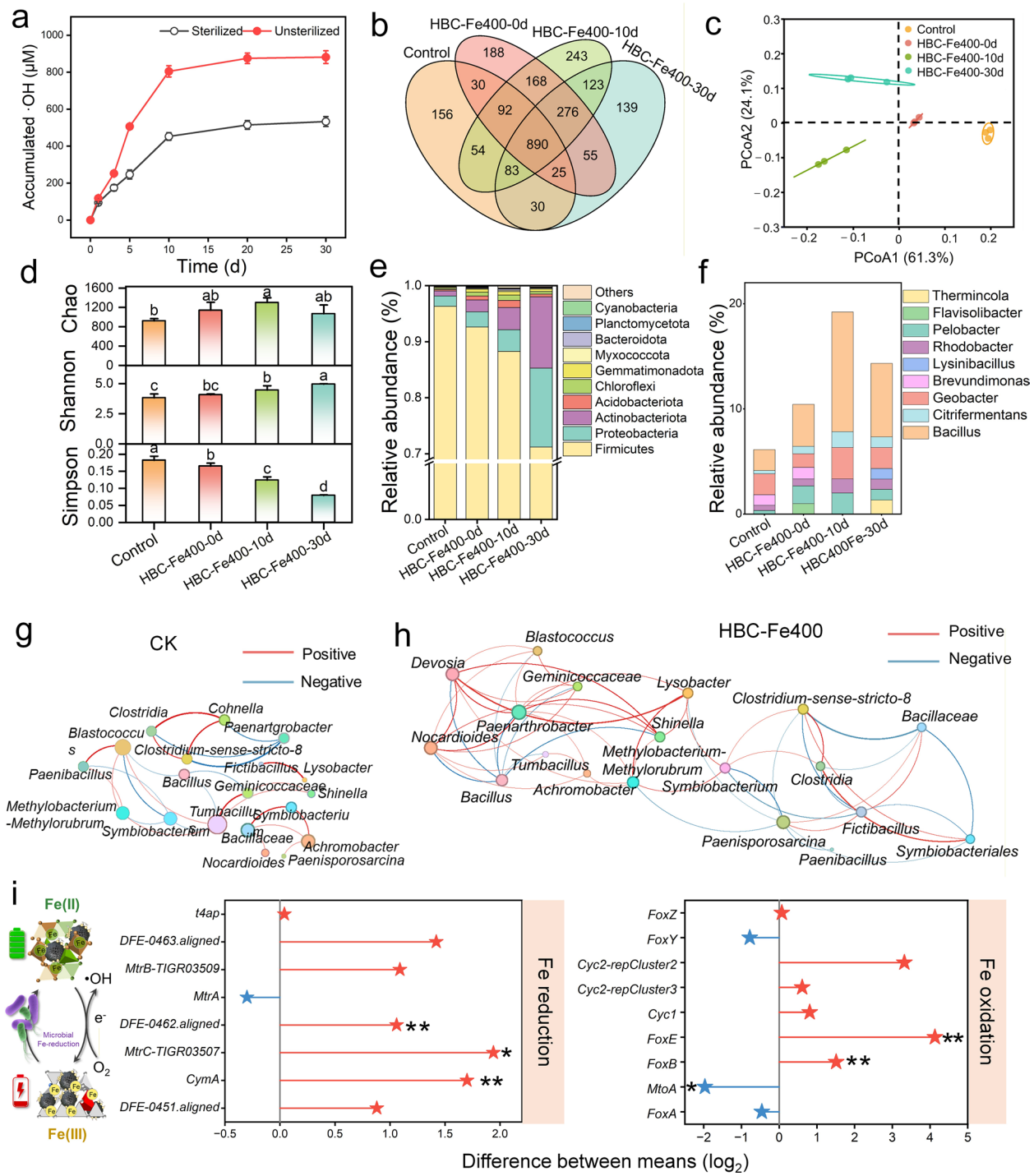

Fig. 4 **a** The accumulation of ·OH in the HBC-Fe400 soil under sterilized and unsterilized conditions. **b** Venn diagram. **c** Principal coordinates analysis of the differences in bacteria microbial communities. **d** Alpha index of bacteria from different soil microcosms. **e** Bacteria microbial responses at the phyla level. **f** Identified Fe(III)-reducing bacteria in the soil. **g**, **h** Co-occurrence networks of microbial communities in CK and HBC-Fe400. **i** Differences in the abundance of functional genes involved in Fe cycling. The values of differences were calculated as "$\log_2$(the mean abundance for a specific gene in the HBC-Fe400 divided by the mean abundance for a specific gene in the Control)". F-test was used to calculate the significance between HBC-Fe400 and control. The asterisk (*) represents p-values (*, $p < 0.05$; **, $p < 0.01$; ***, $p < 0.001$). The data in the control are colored in blue and those for the HBC-Fe400 are colored in red

fluid community interactions. These changes suggest reduced niche partitioning and enhanced interaction potential within the microbial community, reflecting a significant improvement in microbial interconnectivity. Notably, HBC-Fe400 enhanced the positive correlations within the microbial network, thereby confirming the role of cooperative metabolic processes in facilitating the Fenton-like reaction rather than promoting competitive exclusion. Overall, the application of Fe-based biochar can increase the interconnectivity and complexity of microbial communities, demonstrating a significant positive priming effect on the activation of soil Fe-redox cycling, thereby promoting ·OH production for the degradation of pollutants.

Microorganisms can utilize the Fe(II)-Fe(III) as either an electron donor or acceptor in their metabolic processes. Amendment with HBC-Fe400 markedly enriched functional genes associated with both dissimilatory Fe reduction and oxidation in the soil (Fig. 4i). Compared to the unamended control, the HBC-Fe400 treatment showed significant positive $\log_2$ fold changes for key Fe-reducing genes (e.g., *MtrB, MtrC, CymA*). In contrast, the abundance of *MtrA* remained near baseline levels in the control soil, confirming the generally low native potential for microbial Fe(III) reduction. Concurrently, most Fe-oxidizing genes (e.g., *Cyc2-repCluster2, FoxE*) were also significantly more abundant in the HBC-Fe400-amended soil. Although a small number of genes (e.g., *MtoA, FoxA*) were slightly more prevalent in the control, this did not offset the overall enrichment pattern for Fe oxidation. Collectively, these results indicate that HBC-Fe400 stimulated the microbial Fe-redox by concurrently enhancing the genetic potential for both Fe reduction and Fe oxidation, thereby activating a more dynamic and self-sustaining Fe biogeochemical loop in agricultural soil.

3.5 Mechanism of BC-Fe mediated Fe-redox cycling and ·OH formation in soils

As previously mentioned, soil ROS production might be regulated by microbial communities and soil physicochemical properties. To fully comprehend the process

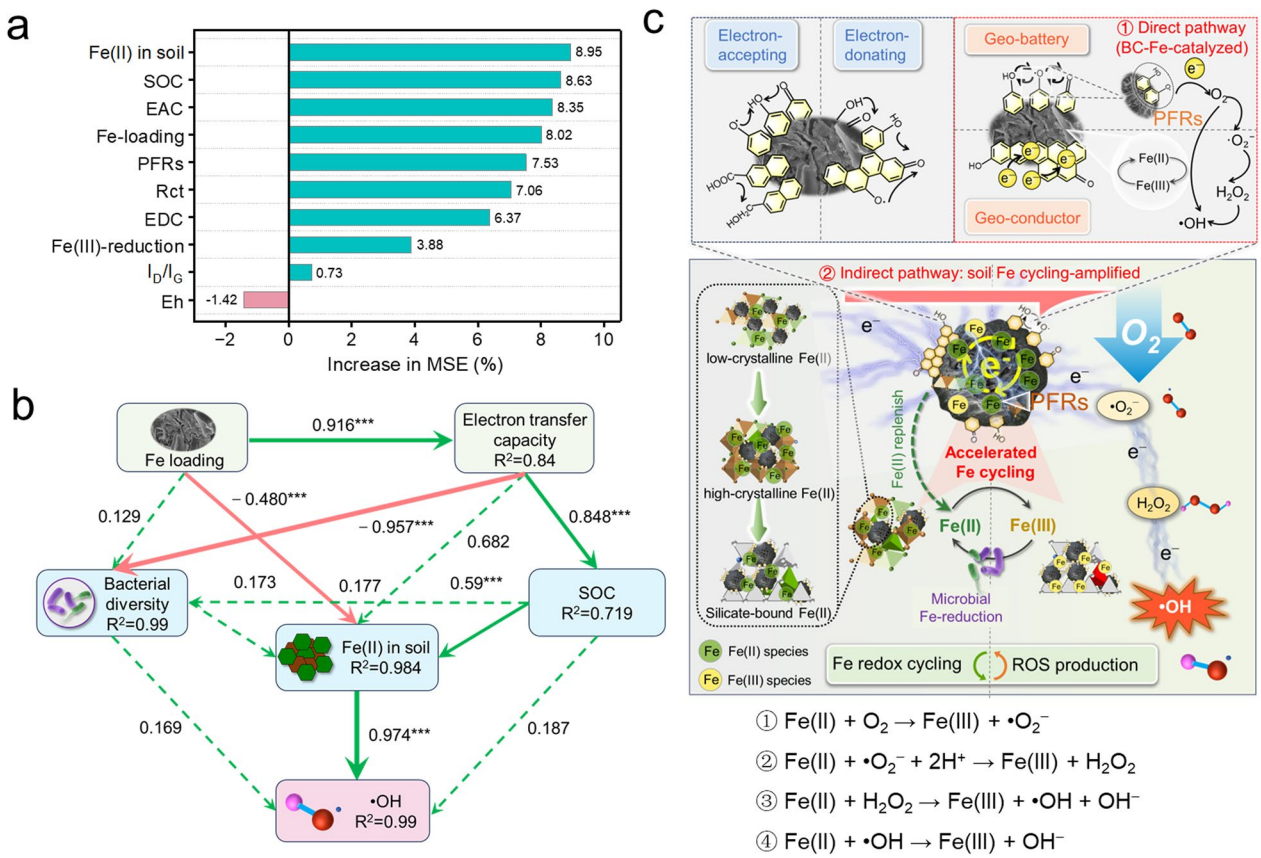

Fig. 5 **a** Random forest model. **b** Identifying the key factors on affecting ·OH formation based on the structural equation model, red and green solid arrows indicate positive and negative correlation, respectively. Red dashed line indicates insignificant correlation ($p > 0.05$). *$p < 0.05$; **$p < 0.01$ and ***$p < 0.001$. $\chi^2 = 0.923$, DF = 4, CFI = 1, GFI = 0.975, RMSEA = 0, $p = 0.921$. **c** Schematic illustration of the mechanisms of the Fe-BC regulating ·OH production and soil remediation processes

of ·OH production in soil, RF model analyses were first employed to identify key factors regulating ·OH production. Based on random forest analysis, it was concluded that the relative contribution of key parameters such as Fe(II) in soil, SOC, EAC, and Fe-loading to ·OH production was 68.03%(Fig. 5a). Simultaneously, the SEM analysis provides quantitative evidence for the plausible mechanisms of soil ·OH production, explaining 99% of the variation(Fig. 5b). Regarding the priming effect of BC-Fe, Fe loading was positively correlated($p < 0.001$) with EEC (path coefficient: 0.92) and soil Fe(II) (0.57), while EEC showed a positive correlation with SOC (0.85) and soil Fe(II) (0.68), suggesting that both Fe loading and EEC of BC-Fe contribute to the soil Fe(II) production, with EEC potentially affecting SOC by facilitating the release of labile organic carbon. Furthermore, the weak positive correlations between Fe-reducing bacteria and soil Fe(II) content may be attributed to the indirect involvement of microbes in Fe(II) formation. Notably, Fe(II) species (0.97) showed a highly positive correlation($p < 0.001$) with ·OH production, in contrast to SOC (0.19) and Fe-reducing bacteria (0.18). This is further supported by the highest standard total effects of Fe(II) species (0.37–0.46),confirming their critical role in promoting ·OH production.

By integrating the priming effect with biotic-abiotic interactions, we propose a comprehensive cross-interface mechanism that governs ·OH production in the soil Fenton-like system. This model emphasizes the spatiotemporal coupling between Fe redox transformations and the electron transfer process, delineating distinct functional zones across the BC-Fex/soil continuum, involving two core stages: Fe(II) formation and Fenton-like oxidation. By constructing biochar with varying Fe loading levels and Fe(II) activities, BC-Fe can gradually release Fe(II) through self-reduction and dissolution processes, meanwhile stimulating the biological Fe(III)-reduction process, thus promoting soil Fe(II) formation and Fe phase transformation for the "charging" of soil geobatteries. Further during Fenton-like oxidation, the electron-storage and electron-conducting properties of biochar, combined with surface-enriched PFRs, can accelerate the electron transfer processes involved in "discharge" of O_2 activation, enhance the efficiency of electron utilization during Fe(II) oxidation, thereby effectively promoting ·OH production. Overall, this dual functionality, regulating Fe(II) species and constructing rapid electron transfer pathways, enables the BC-Fe system to achieve spatiotemporal coordination of biogeochemical processes and enhance ·OH production through the activation of redox-inert soil Fenton-like systems (Fig. 5c).

It is noteworthy that with the increasing Fe loading in BC-Fe, a synergistic interaction developed between "direct" catalysis by BC-Fe and "indirect" oxidation mediated by soil Fe-redox cycling, leading to a substantial enhancement in ·OH production. When the Fe loading reached 10.5% with Fe(II) accounting for 74.6%, the direct Fenton-like catalysis by HBC-Fe400 became increasingly pronounced. This was characterized by a significantly reduced depletion of crystalline Fe(II) in the soil, leading to sustained Fe-redox cycling activation and more rapid and efficient ·OH production. Therefore, this synergy of two-level Fenton-like oxidation, regulated by the BC-Fex physicochemical/ electrochemical properties, as well as the varied spatial distribution of redox-active processes at the mineral-soil interface, enhances the natural cycle by boosting soil Fe(II) release-formation-oxidation to optimize ·OH production for pollutant attenuation.

3.6 SMX degradation induced by dual Fenton-like reaction in soil

3.6.1 SMX Degradation dynamics and contributions

Comprehensive SMX degradation experiments were conducted to evaluate the environmental implications associated with ·OH production (Fig. 6a, b), revealing a two-stage degradation pattern: (1) an initial rapid degradation stage (0–10 days), primarily governed by chemical processes. When O_2 entered the soil, it first reacted with reduced components like Fe(II), thereby activating O_2 to form ·OH radicals and initiating subsequent SMX degradation (Xie et al. 2020; Zhang et al. 2023). This observation aligns with the dynamics of ·OH production and Fe(II) species oxidation, supporting the conclusion that degradation in this stage was mainly driven by ·OH oxidation. (2) The second stage (10–30 days) was characterized by a slower rate of SMX degradation, during which biological processes became dominant. The decrease in oxidative efficiency suggested a diminishing role of chemical oxidation, which was consistent with the gradual increase in ·OH production and enhanced microbial activity. This transition is likely due to BC-Fe aging and the subsequent decreased Fe(III) reduction capacity (Li et al. 2024a).

Comparative analysis of the effects of soil moisture revealed that SMX degradation efficiency reached a maximum of 81% under a 30% water content, while a water-to-soil ratio of 2.5:1 resulted in only 70% degradation. This demonstrates that 30% water content was more favorable for SMX oxidation through Fenton-like reactions. Previous studies have identified the soil–water interface as a hotspot for ROS production, where radical production significantly exceeds that in aqueous phases (Wu et al. 2022). The ·OH production at the interface is an order of magnitude higher than that in bulk water, with this enhancement primarily driven by photochemical processes (Liu et al. 2025). Notably, further experiments

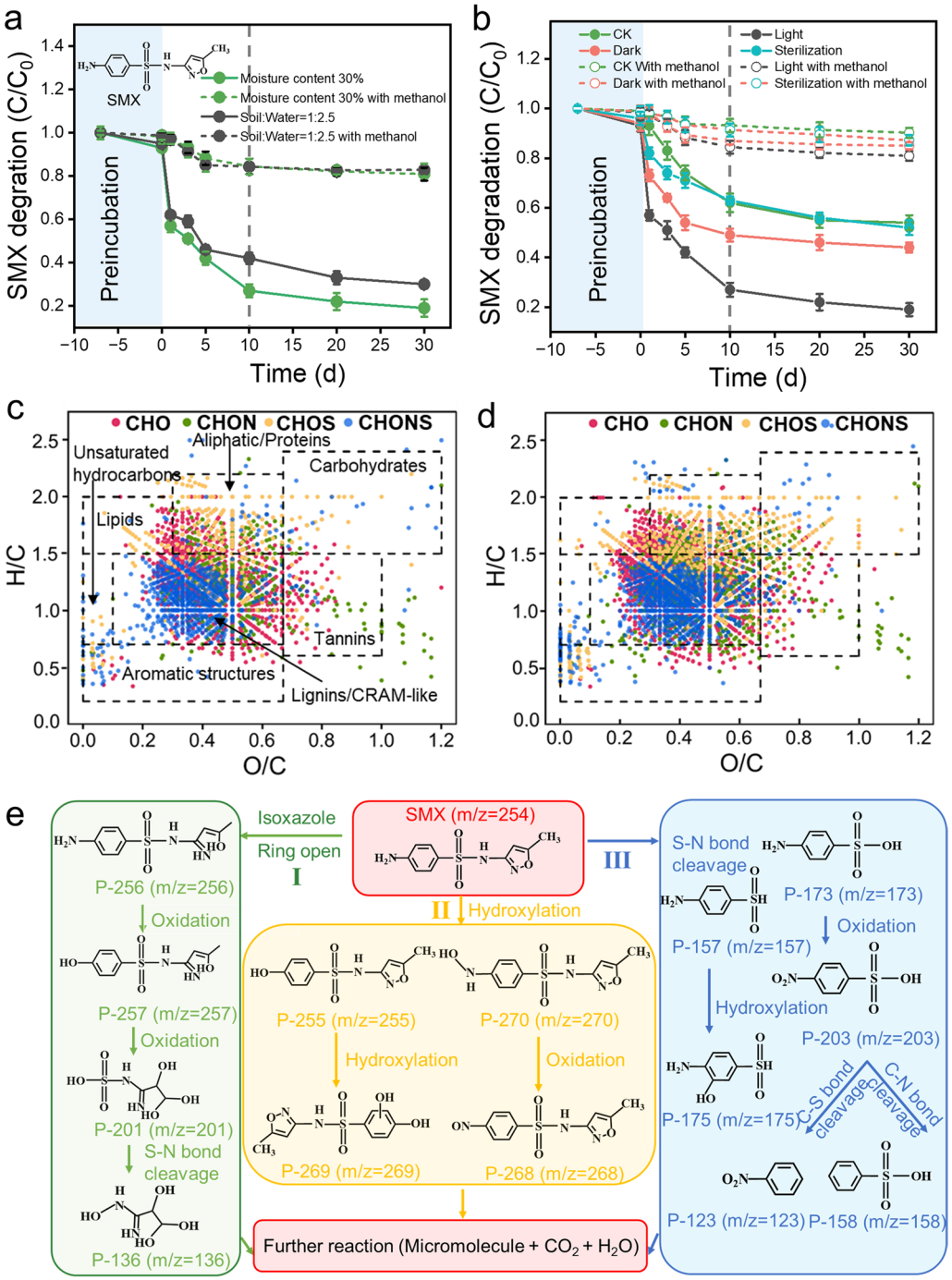

Fig. 6 **a**, **b** Degradation rate of SMX under different conditions in soil. **c**, **d** Van Krevelen diagrams of DOM formulas detected in soils with HBC-Fe400 after 0-,10- and 30-d incubation. **e** Proposed degradation pathways of SMX. Error bars indicate the standard error of three replicates.

conducted under 30% moisture conditions revealed that SMX degradation was most significant (81.2%) under light exposure, markedly higher than in the dark (56.1%), sterilized (48.5%) and Methanol quenching (13.1–17.9%) treatments, suggesting that abiotic processes were the dominant mechanisms driving SMX degradation. However, upon the addition of methanol, a known ·OH scavenger (Chen et al. 2022), the degradation rate dropped drastically to 20%, providing compelling evidence that ·OH radicals played a primary role in SMX degradation.

Notably, Fourier transform ion cyclotron resonance mass spectrometry (FT-ICR-MS) characterization results

demonstrated that the molecular diversity of dissolved organic matter (DOM) increased markedly, from 2517 formulas on day 0 to 3497 on day 10, and reached 4270 by day 30 (Fig. 6c, d and S12). This substantial increase reflects two key processes: (i) SMX degradation generates a variety of intermediates; (ii) HBC-Fe400 modifies native SOM, triggering the formation of new organic species. Furthermore, oxygenation (dominant in 0–10d) elevated O/Cwa (0.395–0.412) via hydroxyl/carboxyl introduction, coinciding with rapid SMX breakdown. Subsequent decarboxylation and deamination reduced N/Cwa (0.105–0.058) and restored H/Cwa (1.231–1.290), while NOSCw shifted from 0.019 to −0.176, indicating the formation of reduced, stable SOM (Fig. S13 and Table S3). This process not only achieves efficient SMX removal but also drives SOM toward more stable, reduced, and diverse molecular forms—demonstrating the potential of this technology for synergistic antibiotic remediation and soil carbon enhancement.

3.6.2 SMX degradation pathways and toxicity assessment

Further degradation intermediates of SMX were monitored using LC–MS. Based on the mass spectral data and intensities presented in Figs. S14 and S15 and table S4, three potential degradation pathways for SMX are proposed and illustrated in Fig. 6e. Pathway I: the isoxazole ring of SMX was first opened to form P-256 (m/z = 256), and then the amino group of P-256 was oxidized to P-257 (m/z = 257). Subsequently, the P-257 underwent ring opening, leading to the formation of P-201 (m/z = 201), ultimately yielding P-136 (m/z = 136) (Chen et al. 2024; Chu et al. 2022; Peng et al. 2022). Pathway II: SMX underwent hydroxylation to form the electrophilic intermediates P-255 (m/z = 255) and P-270 (m/z = 270). P-255 was further hydroxylated to form P-269 (m/z = 269), while the HN-OH portion of P-270 was converted to P-268 (m/z = 268) (Qiu et al. 2024; Wu et al. 2025). Pathway III: The S atom in SMX was attacked, resulting in the cleavage of the S–N bond and the production of

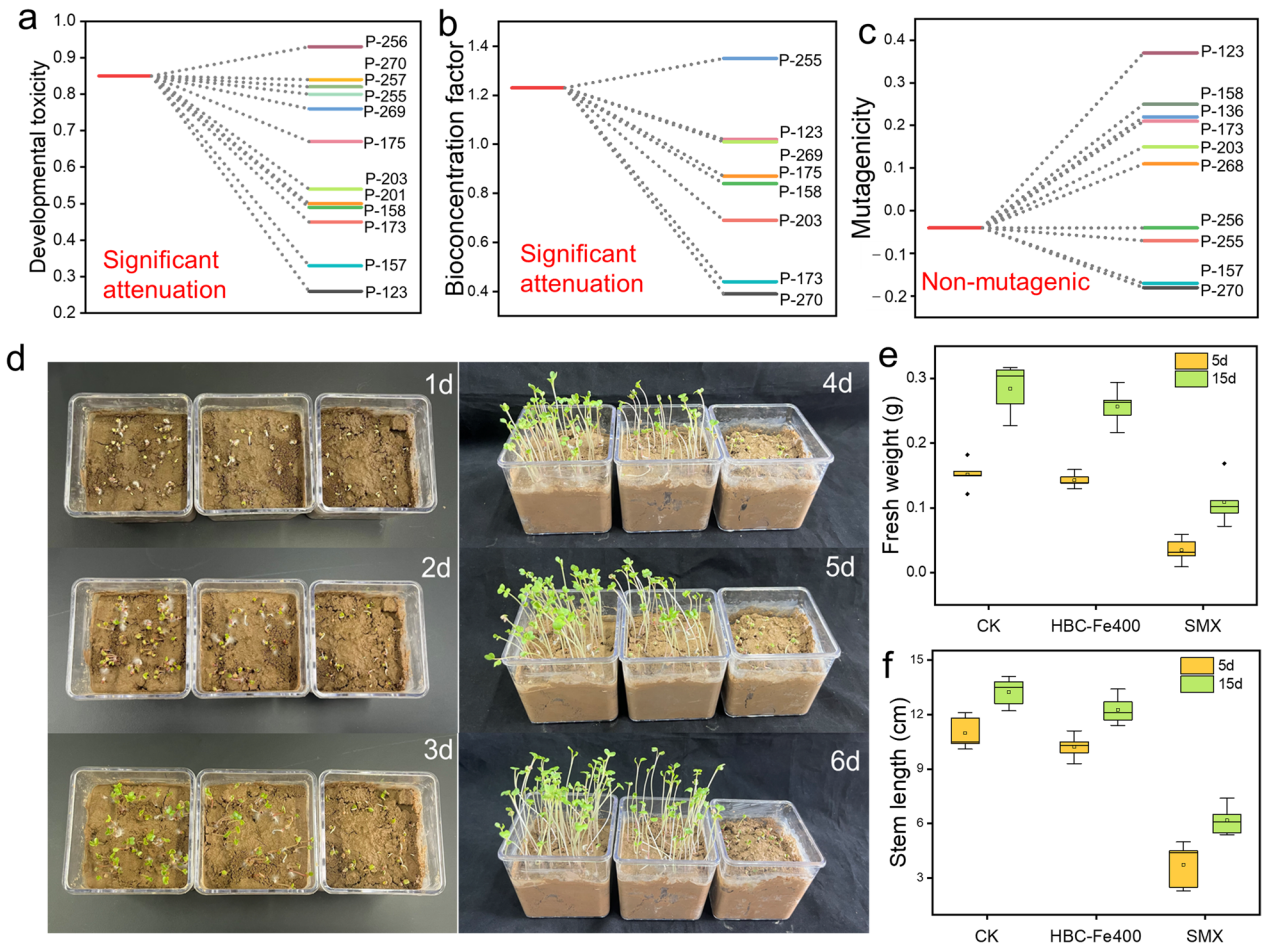

Fig. 7 **a** Developmental toxicity. **b** Bioaccumulation factor. **c** Mutagenicity. **d** The germination rate of cherry radish seeds after application to original soil, HBC-Fe400-remediated soil, and SMX-contaminated soil. **e** Fresh weight. **f** Stem length

P-157 (m/z = 157) and P-173 (m/z = 173). P-173 underwent substitution by surface-bound radicals to form P-175 (m/z = 175), and was oxidized to produce P-203 (m/z = 203). Subsequently, the C-S and C-N bonds of P-203 were oxidized with yielding P-123 (m/z = 123) and P-158 (m/z = 158), respectively (Oyekunle et al. 2022; Zhu et al. 2023).

The toxicity of SMX degradation intermediates was predicted with the Toxicity Estimation Software Tool (T.E.S.T.). As shown in Fig. 7a, b, except for P-256 (m/z = 256) and P-255 (m/z = 255), the developmental toxicity and bioaccumulation potential of the intermediates were lower than those of SMX. Figure 7c shows that all intermediates were non-mutagenic, and their acute toxicity was significantly reduced (Fig. S16). In addition, the germination rate of cherry radish seeds in SMX-contaminated soil was 57%, which was lower than that in uncontaminated soil (99%) and HBC-Fe400-remediated soil (76%) (Fig. 7d). The stem length and fresh weight of the seedlings exhibited a similar trend (Fig. 7e, f).

4 Conclusion

This study demonstrates that the strategic engineering of biochar with optimized Fe speciation and enhanced electron transfer capacity can overcome the fundamental "Fe(II) depletion" bottleneck inherent to soil Fenton-like reactions. The core lies in the creation of a self-sustaining catalytic system: BC-Fe functions as both an "electron highway" and a "Fe-redox cycling hub," achieving spatiotemporally coupled "charging" (microbial Fe(III) reduction) and "discharging" (O_2 activation) processes to drive continuous ·OH generation. Importantly, BC-Fe with optimized Fe loading can minimize the depletion of crystalline Fe(II) while maintaining Fe-redox cycling, through the synchronized activation of both direct (BC-Fe-catalyzed) and indirect (soil Fe-redox cycling-amplified) Fenton-like pathways, thereby promoting green and sustainable soil pollution remediation. This synergistic mechanism moves beyond the study of isolated material catalysis or natural soil processes, representing a new paradigm of "enabling the innate oxidative capacity of soil." The findings not only provide guidance for the BC-Fe-based self-catalysis system to enhance ·OH production, but also offer new insights into the application of in situ remediation technology to improve the productivity and sustainability of sustainable agriculture.

Supplementary Information

The online version contains supplementary material available at https://doi.org/10.1007/s42773-026-00585-0.

Additional file 1.

Acknowledgements
This work was supported by the National Natural Science Foundation of China (Grant No. 42207464), Young Talent Fund of Xi'an Association for Science and Technology (Grant No. 959202413043), Key Research and Development Program of Shaanxi (Grant No. 2025SF-YBXM-511), The Key Industrial Chain Project of Shaanxi Province (2024NC-ZDCYL-02-15) and Natural Science Foundation of Shaanxi Provincial Department of Education (24JK0353).

Author contributions
Hongying Du: Writing-review and editing, Writing-original draft, Visualization, methodology. Lei Zhang: Writing-review and editing, Methodology, Formal analysis, Conceptualization, Funding acquisition. Wenbo Liu: Investigation, Data curation. Yuyang Xie: Investigation, Data curation. Xueyan Hou: Investigation, Data curation. Junkang Guo: Writing-review and editing, conceptualization, funding acquisition. Qixing Zhou: Writing-review and editing, conceptualization, funding acquisition.

Funding
This work was funded by the National Natural Science Foundation of China (Grant No. 42207464), Young Talent Fund of Xi'an Association for Science and Technology (Grant No. 959202413043), Key Research and Development Program of Shaanxi (Grant No. 2025SF-YBXM-511), The Key Industrial Chain Project of Shaanxi Province (2024NC-ZDCYL-02-15) and Natural Science Foundation of Shaanxi Provincial Department of Education (24JK0353).

Data availability
Data will be shared upon reasonable request.

Declarations

Competing interests
The authors declare that they have no known competing financial interests or personal relationships that could have appeared to influence the work reported in this paper.

Author details
[1]School of Environmental Science and Engineering, Shaanxi University of Science and Technology, Xi'an 710021, People's Republic of China. [2]Key Laboratory of Pollution Processes and Environmental Criteria (Ministry of Education)/ Tianjin Key Laboratory of Environmental Remediation and Pollution Control, College of Environmental Science and Engineering, Nankai University, Tianjin 300071, People's Republic of China.

Received: 24 September 2025 Revised: 19 January 2026 Accepted: 23 January 2026
Published online: 11 March 2026

References

Amen R, Bashir H, Bibi I, Shaheen SM, Niazi NK, Shahid M, Hussain MM, Antoniadis V, Shakoor MB, Al-Solaimani SG (2020) A critical review on arsenic removal from water using biochar-based sorbents: the significance of modification and redox reactions. Chem Eng J 396:125195. https://doi.org/10.1016/j.cej.2020.125195

Chen C, Hall SJ, Coward E, Thompson A (2020) Iron-mediated organic matter decomposition in humid soils can counteract protection. Nat Commun 11:2255. https://doi.org/10.1038/s41467-020-16071-5

Chen N, Fu Q, Wu T, Cui P, Fang G, Liu C, Chen C, Liu G, Wang W, Wang D (2021) Active iron phases regulate the abiotic transformation of organic carbon during redox fluctuation cycles of paddy soil. Environ Sci Technol 55:14281–14293. https://doi.org/10.1021/acs.est.1c04073

Chen N, Geng M, Huang D, Tan M, Li Z, Liu G, Zhu C, Fang G, Zhou D (2022) Hydroxyl radical formation during oxygen-mediated oxidation of ferrous iron on mineral surface: dependence on mineral identity. J Hazard Mater 434:128861. https://doi.org/10.1016/j.jhazmat.2022.128861

Chen X, Zhu J, Ma Y, Zeng C, Mu R, Deng Z, Zhang Z (2024) Facile synthesis of ball-milling and oxalic acid co-modified sludge biochar to efficiently activate peroxymonosulfate for sulfamethoxazole degradation: $^1O_2$ and

surface-bound radicals. J Hazard Mater 465:133026. https://doi.org/10.1016/j.jhazmat.2023.133026
Chi J, Liu K, Wu S, Zhang W, Shi Q, Fang L, Li F (2024) Dual-ligand-driven dark reactive oxygen species generation on iron oxyhydroxides: implications for environmental remediation. Environ Sci Technol 58:20751–20760. https://doi.org/10.1021/acs.est.4c08791
Chu Y, Zhang C, Wang R, Chen X, Ren N, Ho SH (2022) Biotransformation of sulfamethoxazole by microalgae: removal efficiency, pathways, and mechanisms. Water Res 221:118834. https://doi.org/10.1016/j.watres.2022.118834
Duan R, Ma S, Ma Y, Xu S, Li G, Fu H, Wu X, Du J, Zhao P (2025) Efficient inactivation of antibiotic resistant bacteria by iron-modified biochar and persulfate system: potential for controlling antimicrobial resistance spread and mechanism insights. J Hazard Mater 492:138182. https://doi.org/10.1016/j.jhazmat.2025.138182
Han R, Wang Z, Lv J, Zhu Z, Yu G-H, Li G, Zhu Y-G (2022) Multiple effects of humic components on microbially mediated iron redox processes and production of hydroxyl radicals. Environ Sci Technol 56:16419–16427. https://doi.org/10.1021/acs.est.2c03799
He H, Liu J, Shu Z, Chen Y, Pan Z, Peng C, Wang X, Zhou F, Zhou M, Du Z (2024) Microbially driven iron cycling facilitates organic carbon accrual in decadal biochar-amended soil. Environ Sci Technol 58:12430–12440. https://doi.org/10.1021/acs.est.3c09003
Huang D, Chen N, Lin Y, Ge C, Wang X, Wang D, Zhu C, Fang G, Zhou D (2023a) Pyrogenic carbon accelerates iron cycling and hydroxyl radical production during redox fluctuations of paddy soils. Biochar 5:3–17. https://doi.org/10.1007/s42773-023-00236-8
Huang D, Chen N, Zhu C, Sun H, Fang G, Zhou D (2023b) Dynamic production of hydroxyl radicals during the flooding-drainage process of paddy soil: an in situ column study. Environ Sci Technol 57:16340–16347. https://doi.org/10.1021/acs.est.3c04967
Huang J, Jones A, Waite TD, Chen Y, Huang X, Rosso KM, Kappler A, Mansor M, Tratnyek PG, Zhang H (2021) Fe (II) redox chemistry in the environment. Chem Rev 121:8161–8233. https://doi.org/10.1021/acs.chemrev.0c01286
Huang R, Lu X, Li W, Xiong J, Yang J (2024) Progress on the adsorption characteristics of nZVI and other iron-modified biochar for phosphate adsorption in water bodies. Circ Econ 3:100112. https://doi.org/10.1016/j.cec.2024.100112
Li C, Zhang Y, Zheng Y, Shi C, Lu Y, Zhang Y, Yuan S (2024a) Contaminant transformation during sediment oxygenation: temporal variation of oxidation mechanisms mediated by hydroxyl radicals and aerobic microbes. Sci Total Environ 919:170855. https://doi.org/10.1016/j.scitotenv.2024.170855
Li D, Sun J, Fu Y, Hong W, Wang H, Yang Q, Wu J, Yang S, Xu J, Zhang Y (2024b) Fluctuating redox conditions accelerate the electron storage and transfer in magnetite and production of dark hydroxyl radicals. Water Res 248:120884. https://doi.org/10.1016/j.watres.2023.120884
Li X, Tan M, Wu B, Wang J, Ma J, Chen B, Chu C (2024c) Redox oscillation-driven production of reactive oxygen species from black carbon. Environ Sci Technol 58:21210–21217. https://doi.org/10.1021/acs.est.4c09102
Liu F, Ding Y, Liu J, Latif J, Qin J, Tian S, Sun S, Guan B, Zhu K, Jia H (2024a) The effect of redox fluctuation on carbon mineralization in riparian soil: an analysis of the hotspot zone of reactive oxygen species production. Water Res 265:122294. https://doi.org/10.1016/j.watres.2024.122294
Liu F, Wang Z, Liu J, Latif J, Qin J, Yang H, Jiang W, Deng Y, Yang K, Ni Z (2024b) Seasonal and spatial fluctuations of reactive oxygen species in riparian soils and their contributions on organic carbon mineralization. Environ Sci Technol 58:7066–7077. https://doi.org/10.1021/acs.est.3c10756
Liu J, Zhu C, Zhu F, Sun H, Wang J, Fang G, Zhou D (2024c) Strong substance exchange at paddy soil-water interface promotes nonphotochemical formation of reactive oxygen species in overlying water. Environ Sci Technol 58:7403–7414. https://doi.org/10.1021/acs.est.3c10866
Liu X, Huang D, Zhu C, Zhu F, Zhu X, Zhou D (2024d) Production of reactive oxygen species during redox manipulation and its potential impacts on activated sludge wastewater treatment processes. Environ Sci Technol 58:23042–23052. https://doi.org/10.1021/acs.est.4c11301
Liu X, Pan Y, Yao Y, Chen S, Chen B, Chu C (2025) Accelerated pollutant degradation by UV/H_2O_2 at the air-water interface of microdroplets. Environ Sci Technol 59:5406–5414. https://doi.org/10.1021/acs.est.4c14592
Mcdonald-Wharry J, Manley-Harris M, Pickering K (2013) Carbonisation of biomass-derived chars and the thermal reduction of a graphene oxide sample studied using Raman spectroscopy. Carbon 59:383–405. https://doi.org/10.1016/j.carbon.2013.03.033
Meng F, Tong H, Feng C, Huang Z, Wu P, Zhou J, Hua J, Wu F, Liu C (2024) Structural Fe (II)-induced generation of reactive oxygen species on magnetite surface for aqueous As (III) oxidation during oxygen activation. Water Res 252:121232. https://doi.org/10.1016/j.watres.2024.121232
Oyekunle DT, Gendy EA, Ifthikar J, Chen Z (2022) Heterogeneous activation of persulfate by metal and non-metal catalyst for the degradation of sulfamethoxazole: a review. Chem Eng J 437:135277. https://doi.org/10.1016/j.cej.2022.135277
Peng W, Liao J, Yan Y, Chen L, Ge C, Lin S (2022) Enriched nitrogen-doped carbon derived from expired drug with dual active sites as effective peroxymonosulfate activator: ultra-fast sulfamethoxazole degradation and mechanism insight. Chem Eng J 446:137407. https://doi.org/10.1016/j.cej.2022.137407
Qiu Y, Huang Y, Wang Y, Liu X, Huang D (2024) Facile synthesis of Cu-doped manganese oxide octahedral molecular sieve for the efficient degradation of sulfamethoxazole via peroxymonosulfate activation. Int J Min Met Mater 31:2770–2780. https://doi.org/10.1007/s12613-024-2858-z
Shen L, Zhu X, Jiang H, Zhang J, Chen C, R. Reinfelder J, Kappler A, Fang L, Liu T, Liu C (2025) Physical contact between bacteria and carbonaceous materials: the key switch triggering activated carbon and biochar to promote microbial iron reduction. Environ Sci Technol 59:9576–9586. https://doi.org/10.1021/acs.est.4c14024
Si T, Chen X, Yuan R, Pan S, Wang Y, Bian R, Liu X, Zhang X, Joseph S, Li L (2024) Iron-modified biochars and their aging reduce soil cadmium mobility and inhibit rice cadmium uptake by promoting soil iron redox cycling. J Environ Manage 370:122848. https://doi.org/10.1016/j.jenvman.2024.122848
Tao S, Yang J, Hou H, Liang S, Xiao K, Qiu J, Hu J, Liu B, Yu W, Deng H (2019) Enhanced sludge dewatering via homogeneous and heterogeneous Fenton reactions initiated by Fe-rich biochar derived from sludge. Chem Eng J 372:966–977. https://doi.org/10.1016/j.cej.2019.05.002
Thomasarrigo LK, Notini L, Vontobel S, Bouchet S, Nydegger T, Kretzschmar R (2024) Emerging investigator series: coprecipitation with glucuronic acid limits reductive dissolution and transformation of ferrihydrite in an anoxic soil. Environ Sci Process Impacts 26:1489–1502. https://doi.org/10.1039/d4em00238e
Wan D, Liu FF, Chen JB, Kappler A, Kuzyakov Y, Liu CQ, Yu GH (2022) Microbial community mediates hydroxyl radical production in soil slurries by iron redox transformation. Water Res 220:118689. https://doi.org/10.1016/j.watres.2022.118689
Wang D, Huang D, Wu S, Fang G, Zhu F, Chen N, Liu S, Zhu C, Zhou D (2021) Pyrogenic carbon initiated the generation of hydroxyl radicals from the oxidation of sulfide. Environ Sci Technol 55:6001–6011. https://doi.org/10.1016/j.jes.2023.11.023
Wang J, Cai J, Zhou X, Wang S, Luo F, Yang L, Yu J, Chi R, Chen Z (2025a) Accelerating of Fe^{2+} regeneration in Fenton reaction by biochar: pivotal roles of carbon defects as electron donor and shuttle. Sep Purif Technol 354:128945. https://doi.org/10.1016/j.seppur.2024.128945
Wang Y, Ning X, Liang J, Wang A, Qu J (2025b) Enhancing microbial superoxide generation and conversion to hydroxyl radicals for enhanced bioremediation using iron-binding ligands. J Environ Sci 147:597–606. https://doi.org/10.1016/j.jes.2023.11.023
Wei W, Wen X, Zhang S, Lin L, Zhu J, Yu J, Li J, Lou Z, Xu X (2025) Co-governance of iron speciation and carbon phase on Fenton-like reaction triggered by Fe-enriched industrial sludge derived biochar. J Clean Prod 486:144516. https://doi.org/10.1016/j.jclepro.2024.144516
Wu B, Zhou C, Zhao G, Wang J, Dai H, Liu T, Zheng X, Chen B, Chu C (2022) Enhanced photochemical production of reactive intermediates at the wetland soil-water interface. Water Res 223:118971. https://doi.org/10.1016/j.watres.2022.118971
Wu P, Luo Y, Hu T, An X, Xu X, Sun L, Tang T, Fan J (2025) Sustainable biodegradation of triclosan and sulfamethoxazole with cyanobacteria: resistance mechanism and metabolic transformation. ACS EST Water. https://doi.org/10.1021/acsestwater.4c00975
Xia W, Li S, Wu G, Ma J (2023) Recycling waste iron-rich algal flocs as cost-effective biochar activator for heterogeneous Fenton-like reaction towards tetracycline degradation: important role of iron species and moderately defective structures. J Hazard Mater 460:132377. https://doi.org/10.1016/j.jhazmat.2023.132377

Xiao F, Wang Z, Fan J, Majima T, Zhao H, Zhao G (2021) Selective electrocatalytic reduction of oxygen to hydroxyl radicals via 3-electron pathway with FeCo alloy encapsulated carbon aerogel for fast and complete removing pollutants. Angew Chem Int Ed 60:10375–10383. https://doi.org/10.1002/anie.202101804

Xie W, Yuan S, Tong M, Ma S, Liao W, Zhang N, Chen C (2020) Contaminant degradation by ·OH during sediment oxygenation: dependence on Fe (II) species. Environ Sci Technol 54:2975–2984. https://doi.org/10.1021/acs.est.9b04870

Xie W, Zhang P, Liao W, Tong M, Yuan S (2021) Ligand-enhanced electron utilization for trichloroethylene degradation by ·OH during sediment oxygenation. Environ Sci Technol 55:7044–7051. https://doi.org/10.1021/acs.est.1c00136

Xu L, Fu B, Sun Y, Jin P, Bai X, Jin X, Shi X, Wang Y, Nie S (2020) Degradation of organic pollutants by Fe/N co-doped biochar via peroxymonosulfate activation: synthesis, performance, mechanism and its potential for practical application. Chem Eng J 400:125870. https://doi.org/10.1016/j.cej.2020.125870

Xu Z, Wan Z, Sun Y, Gao B, Hou D, Cao X, Komárek M, Ok YS, Tsang DC (2022) Electroactive Fe-biochar for redox-related remediation of arsenic and chromium: distinct redox nature with varying iron/carbon speciation. J Hazard Mater 430:128479. https://doi.org/10.1016/j.jhazmat.2022.128479

Yang H, Chen N, Wang Z, Liu J, Qin J, Zhu K, Jia H (2023) Biochar-associated free radicals reduce soil bacterial diversity: new insight into ecoenzymatic stoichiometry. Environ Sci Technol 57:20238–20248. https://doi.org/10.1021/acs.est.3c06864

Yang K, Liu J, Wang Z, Zhu K, Jia B, Yang H, Qin J, Xie J, Latif J, Liu F (2025) Spatiotemporal dynamics of reactive oxygen species in the detritusphere and their critical roles in organic carbon mineralisation. Soil Biol Biochem 202:109700. https://doi.org/10.1016/j.soilbio.2024.109700

Yang Z, Sun T, Kleindienst S, Straub D, Kretzschmar R, Angenent LT, Kappler A (2021) A coupled function of biochar as geobattery and geoconductor leads to stimulation of microbial Fe (III) reduction and methanogenesis in a paddy soil enrichment culture. Soil Biol Biochem 163:108446. https://doi.org/10.1016/j.soilbio.2021.108446

Yu C, Ji W, Li X, Yuan S, Zhang P, Pu S (2024) Critical role of mineral Fe (IV) formation in low hydroxyl radical yields during Fe (II)-bearing clay mineral oxygenation. Environ Sci Technol 58:9669–9678. https://doi.org/10.1021/acs.est.3c09986

Zhu B, Yu Y, Ding Y, Ge S (2024) Iron-modified granular sludge biochar-based catalysts for improved Rhodamine B degradation by activating peroxymonosulfate. Biomass Convers Biorefin 14:27755–27765. https://doi.org/10.1007/s13399-022-03340-0

Zhang P, Liu J, Yu H, Cheng D, Liu H, Yuan S (2023) Kinetic models for hydroxyl radical production and contaminant removal during soil/sediment oxygenation. Water Res 240:120071. https://doi.org/10.1016/j.watres.2023.120071

Zhao G, Tan M, Wu B, Zheng X, Xiong R, Chen B, Kappler A, Chu C (2023) Redox oscillations activate thermodynamically stable iron minerals for enhanced reactive oxygen species production. Environ Sci Technol 57:8628–8637. https://doi.org/10.1021/acs.est.3c02302

Zhang S, Wei Y, Metz J, He S, Alvarez PJ, Long M (2022) Persistent free radicals in biochar enhance superoxide-mediated Fe (III)/Fe (II) cycling and the efficacy of CaO2 fenton-like treatment. J Hazard Mater 421:126805. https://doi.org/10.1016/j.jhazmat.2021.126805

Zhu K, Qin W, Gan Y, Huang Y, Jiang Z, Chen Y, Li X, Yan K (2023) Acceleration of Fe^{3+}/Fe^{2+} cycle in garland-like MIL-101 (Fe)/MoS_2 nanosheets to promote peroxymonosulfate activation for sulfamethoxazole degradation. Chem Eng J 470:144190. https://doi.org/10.1016/j.cej.2023.144190